Proceedings of 12th Cambridge Workshop on Cool Stars, Stellar Systems, & The Sun, 2003 University of Colorado.

Buoyant Magnetic Flux Ropes and Convection: Evolution Prior to Emergence

S.B.F. Dorch

The Royal Swedish Academy of Sciences

Abstract.
We have performed detailed numerical 3-d simulations of the interaction of buoyantly ascending twisted magnetic flux ropes and solar-like stratified convection (with surface cells similar to solar supergranules in size). Results are presented for three different cases — corresponding to different amounts of initial field line twist — that represents fundamentally different types of instabilities: the magnetic Rayleigh-Taylor instability in which case the flux rope disrupts and network patches are formed at surface cell boundaries; the kink instability that has been proposed as a mechanism for forming tightly packed δ-type spots; a stable flux rope where neither of the former instabilities arise, and the behavior of which is similar to classical text book flux tubes, except from a flux-loss due to the advective action of the convective flows. The simulations thus support the idea that the magnetic flux observed at the surface in bipolar regions are smaller, ceteris paribus, than that of the dynamo generated flux ropes near the bottom of the convection zone. Please note that this material is also available as an online web-talk.

1. Introduction

Buoyant magnetic flux tubes are an essential part of the framework of the current theories of dynamo action in stars, in particular in the case of cool dwarf stars such as the Sun, that has outer convection zones. Models of buoyant magnetic flux tubes that are based on the essentially 1-d thin flux tube approximation are consistent with the observed latitudes of emergence and tilt angles of bipolar magnetic regions on the surface of the Sun, if the initial field strength of the tubes are of the order of 10 times the convection equipartition value (Fan et al. 1994 and Caligari et al. 1995).

More general 2-d simulations of flux tube cross-sections, not relying on the assumption that the flux tubes are thin, have shown that purely cylindrical tubes are disrupted by the magnetic Rayleigh-Taylor (R-T) instability, rendering them unlikely to reach the surface (Emonet & Moreno-Insertis 1998, Dorch & Nordlund 1998, and several others). This is a result of the too simple topology assumed for the magnetic field of these flux tubes: rather, the magnetic field line tension present in a twisted flux rope suppresses the R-T instability and hence prevents the flux ropes from disintegrating as it has been demonstrated by e.g. Emonet & Moreno-Insertis (1998). Recently, 3-d simulations of buoyant twisted flux loops have confirmed that several of the results found in the 2-d simulations carry over to the more realistic 3-d scenario (Dorch et al. 1999): on the one hand, the apex cross-sections of twisted flux loops are well described by the 2-d studies and the S-shaped structure of a twisted flux loop as it emerges through the upper computational boundary is qualitative similar to the sigmoidal structures observed in EUV and soft X-ray by the Yohkoh and SoHO satellites (e.g. Sterling et al. 2000). On the other hand, it has been suggested that the value of the critical degree of twist needed to prevent the R-T instability may be unrealistically high in the 2-d case, and a smaller twist may be sufficient in the case of sinusoidal 3-d magnetic flux loops as in the simulations of Abbett et al. (2000). So far, a lot of questions remain unanswered, e.g. whether the quasi-steady state topology that the flux ropes reach in the later phase of their rise in 2-d simulations (e.g. Emonet & Moreno-Insertis 1998 and Dorch et al. 1999) is stable towards perturbations from the surroundings, and whether the results found for 3-d flux ropes moving in a 1-d average static stratification, at all are valid in the more realistic case.

Here I present first results on the behavior of buoyantly rising twisted flux ropes in a dynamical "background" environment, namely by including a model of a convection zone (CZ) with solar-like supergranulation. It is not my aim to describe an extensive parameter study the results of which would be dependent on the particular toy model of solar convection that we are using. Rather the intend is to examine how one may expect the inclusion of convection to change previous conclusions on the properties of buoyant magnetic flux ropes rising within the Sun.

2. Model

The initial set-up of the model is twofold, consisting of a snapshot of a solar-like CZ, and of an idealized twisted magnetic flux rope. The model has a higher luminosity than the Sun to avoid problems with the large ratio of the thermal to dynamical time scales, and all variables are scaled to compare to solar values.

The full MHD-equations are solved on a grid of 150 vertical times 105^2 horizontal grid points, using the computational method by Galsgaard and others (Galsgaard & Nordlund 1997, and Nordlund, Galsgaard & Stein 1994), employing a finite difference staggered mesh with 6th order derivative operators, 5th order centering operators and a 3rd order time-stepping routine. In this scheme the viscous and magnetic diffusive terms are quenched in regions with smooth variations, to reduce the diffusion of well-resolved structures. Typical magnetic Reynolds numbers in non-smooth regions are of the order of a few hundred, while several orders of magnitude higher in the smooth regions.

2.1. Boundary conditions

In solar-like cool stars convection is essentially driven by cooling at a thin surface layer. To model this without including all the layers up to the actual surface, a simple expression for an isothermal cooling layer at the upper boundary of the model is used, restricting the effect to a thin layer. This layer is, however, far below the real boundary of the solar CZ. Horizontally the boundaries are periodic.

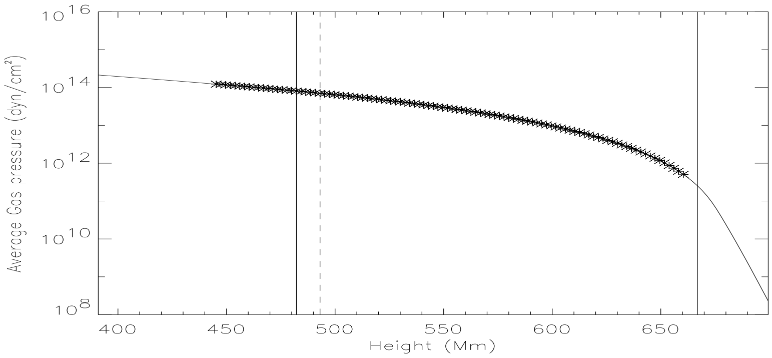

Figure 1. The average pressure stratification of the initial hydrodynamic convection model. The over-plotted part (stars) corresponds to the range of the polytropic reference simulations. The vertical solid lines denotes the bottom and top of the CZ and the vertical dashed line indicates the initial position of the magnetic flux rope.

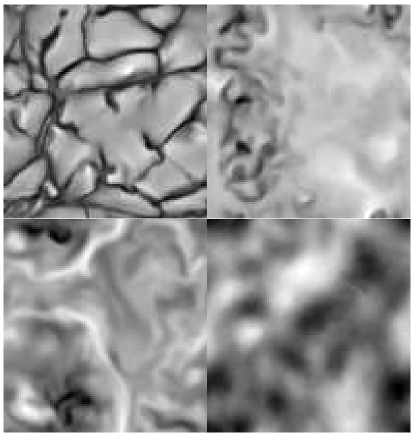

Figure 2. The vertical velocity in horizontal slices of the model convection zone in the initial state at four different heights: at the surface (upper left) and middle (upper right) layers of the convection zone, at the initial depth of the flux rope (lower left) and at a layer below the CZ (lower right).

2.2. Hydrodynamic initial condition

The hydrodynamic part of the initial condition is a snapshot from a well developed stage of a numerical "toy model" of deep solar-like convection with a gas pressure contrast of roughly 2.5 orders of magnitude in the CZ alone (see Fig 1). The physical size of the computational box is 250 Mm in the horizontal direction and 313 Mm in the vertical.

As typical for over-turning stratified hydrodynamic convection, a cellular granulation pattern is generated on the CZ's surface (see Fig 2). The typical length scale of this pattern is about 50 Mm, somewhat larger than the canonical size of solar supergranules. Scaled to the Sun, the typical velocity of this granulation is about 200 m/s in the narrow downdrafts at the surface and slightly less in the larger upwelling regions, close to what is found for solar supergranulation.

2.3. Magnetic initial condition

Initially the entropy in the interior of the rope is set equal to that in the external medium. This corresponds to buoyancy a factor of $1/\gamma$ (with $\gamma = 5/3$) lower than in the case of temperature balance where the buoyancy has the classical value of $1/\beta$. The initial twist of the flux ropes is given by

$$\mathrm{B}_z = \mathrm{B}_0 e^{-(r/\mathrm{R})^2} \text{ and } \mathrm{B}_\phi = \alpha r/\mathrm{R}\ \mathrm{B}_z, \tag{1}$$

where B_z is the parallel and B_ϕ the transversal component of the magnetic field with respect to the rope's main axis. B_0 is the amplitude of the field and R the radius. The coordinate system is chosen so that x is the vertical coordinate and z the coordinate along the axis which initially is parallel to the rope. The position of the rope is described by the set (x_c, y_c), initially equal to (x_0, y_0), where the points $(x_c(z), y_c(z))$ along the z-axis are the positions in the (x, y) plane, where B_z is maximum for a given z-value — these positions define the flux rope's axis in the following.

An expression similar to Eq. (1) has been applied in both 2-d and 3-d simulations and it has been shown that for these cases the R-T instability is inhibited if the degree of twist is sufficiently high (Emonet & Moreno-Insertis 1998). This kind of topology is simple but similar to the relaxed state of a flux rope with a more complicated topology used in Dorch & Nordlund (1998).

The wavelength λ of the flux rope is equal to the horizontal size of the domain so that $\lambda = 3.2\ \mathrm{H_{P0}}$ at the initial position of the rope where the pressure scale height is $\mathrm{H_{P0}} = 78.3$ Mm. Then the flux rope is not undular Parker-unstable even though the stratification admits this instability for ropes longer than a critical wavelength of $\sim 12\ \mathrm{H_{P0}}$. Initially the ropes are twisted, with a maximum pitch angle of $\psi_\mathrm{R} = \arctan(\alpha)$. In the following we set the initial radius $\mathrm{R}_0 = 0.177\ \mathrm{H_{P0}}$.

The high luminosity of the model poses both pros and cons when choosing the magnetic field strength: on the one hand, the ratio of kinetic to thermal energy density e_K/e is much larger in the model than it is in the Sun. Then β_0 must be chosen to be smaller than what is the case for the magnetic field at the bottom of the CZ, in order that the ratio of magnetic to kinetic energy density $e_\mathrm{M}/e_\mathrm{K}$ to be of the right order of magnitude (which is about 100 in the case of the Sun). On the other hand, from a computational point of view one would anyhow have to set β_0 lower than the solar values (10^4 – 10^7) to reduce the computational time-scale to a reasonable value. As a compromise we choose the initial field strength to be given by $\beta_0 = 100$ which yields $e_\mathrm{M}/e_\mathrm{K} = 100$.

The initial position of the ropes in the CZ is significant for the subsequent detailed history of their rise: with the present flows and location of the flux ropes, most parts of the ropes are located inside or close to a convective updraft.

Thus, the ascent of the ropes are influenced by this, and we cannot draw any conclusions on the detailed path of rise.

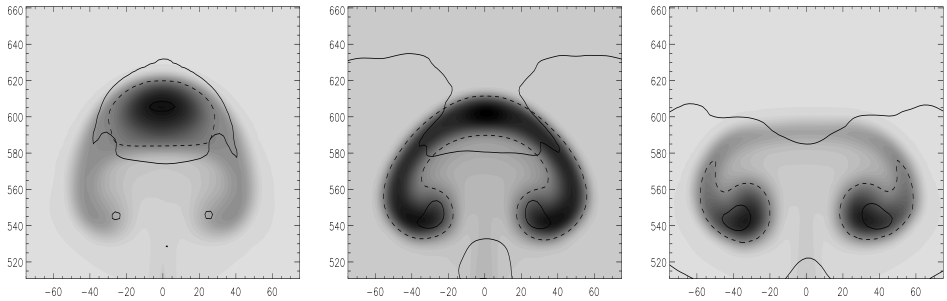

Figure 3. Images showing B_z at time 67.7 τ_A in the 2-d reference simulations for $\psi_R = 30^o, 20^o$ and 10^o (left to right). Shown by contours are the equipartition curves. Also shown are HWHM-contours of B_z (dashed). Only part of the computational box is shown.

3. Two-dimensional Reference Simulations

For reference we have performed a number of 2-d simulations for several values of β_0 and ψ_R. These reference simulations lack convection and have a polytropic atmosphere chosen by calculating the mass density $\rho(x)$ from the average gas pressure $P(x)$ in the 3-d hydrodynamic convection model via $P = P_0(\rho/\rho_0)^\gamma$, where P_0 and ρ_0 are the average quantities at the initial position of the flux rope (see Fig 1).

The results of these reference simulations agree perfectly with previous 2-d studies: e.g. the ropes are disrupted by the R-T instability unless their pitch angle exceeds a critical value. As the ropes rise and expand they enter a "terminal rise phase" where they ascent with a constant speed before they reach the upper computational boundary. In this phase the speed is the so-called terminal velocity v_t determined by the balance between buoyancy and drag. In the reference simulation with $\psi_R = 30^o$ we get $v_t \approx 0.1\ v_{A0}$ (with v_{A0} being the Alfvén speed v_A at $x_c = x_0$). The largest Mach number reached during the entire rise is 8.5×10^{-2}, so that the motions are completely sub-sonic. The characteristic time scale of the ascent then becomes $\tau_{rise} = H_{P0}/v_t \approx 50\ \tau_A$ with $\tau_A = R_0/v_{A0}$.

The boundary of a flux rope can be defined by the equipartition curve (the locations where the transversal magnetic field is in equipartition with the kinetic energy relative to the rise of the rope). Fig 3. shows equipartition curves for three values of ψ_R: only the most twisted ropes withstand the exterior pressure fluctuations, and the transversal field is strong enough to protect the buoyant core of the flux rope. From the simulations we find that a minimum pitch angle in the range 25^o – 30^o is required for the ropes to be unaffected by the R-T instability.

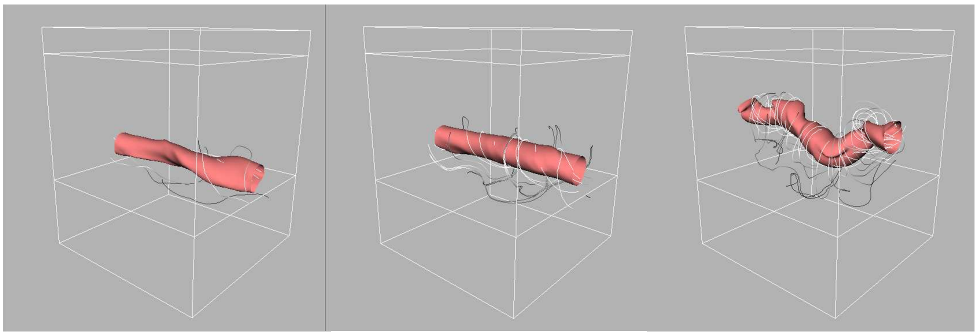

Figure 4. Snapshots of magnetic field isosurfaces at time $t = 28\ \tau_{\mathrm{A}}$ for the simulations 3D25, 3D45 and 3D75 (left to right): the magnetic field isosurfaces are outline the HWHM surfaces.

4. Results

In the following we discuss results from three different convective 3-d simulations distinguished only by the value of the pitch parameter α, and thus ψ_{R}. These three cases adhere to different regimes with respect to the onset of instabilities (Fig 4): the case henceforth denoted 3D75 ($\psi_{\mathrm{R}} = 75^{\mathrm{o}}$) is kink unstable, but stable towards the R-T instability. 3D25 ($\psi_{\mathrm{R}} = 25^{\mathrm{o}}$) is stable towards the kink instability, but marginally R-T unstable. The case 3D45 ($\psi_{\mathrm{R}} = 45^{\mathrm{o}}$) is stable towards both instabilities. Only the behavior of the ropes during the initial and rise phases are discussed. When the ropes approach the upper boundary of the CZ, they enter an "emergence phase" beyond the scope of this contribution.

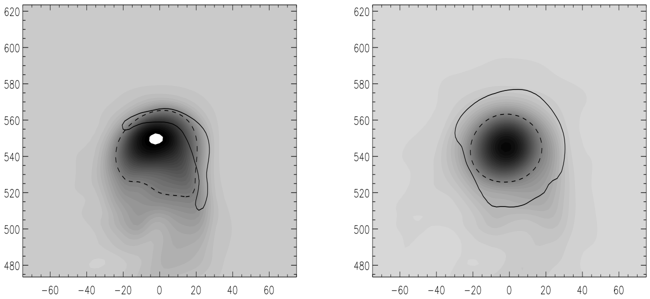

Figure 5. Two average cross-sectional snapshots of B_z (gray scale) and the equipartition curve at time $= 35.6\ \tau_{\mathrm{A}}$ in simulations 3D25 (left) and 3D45 (right). Also shown are the HWHM-contours (dashed) (quantities are averages along the rope). Only part of the computational box is shown.

4.1. The Rayleigh-Taylor instability

Consider the case 3D25, where the pitch is far to low to excite the kink instability, but where we refind the R-T instability in addition to the action of the convective flows. Fig 5. shows cross-sectional averages of the magnetic field in 3D25 and 3D45 which may be compared to the corresponding images in Fig 3: in the 2-d case, the horizontal and vertical sizes of the ropes do not increase equally fast. This effect is primarily because of the differential buoyancy that squeezes the ropes in the vertical direction, and by flux conservation, expands them horizontally. The effect is less apparent in 3-d, where the ropes are more circular (see Fig 5) when defined by the HWHM-boundary. The equipartition curve, however, loses its 2-d symmetry. As the rope rises and the R-T instability sets in, the flux rope disrupts and eventually fills the bulk of the CZ. At late stages the magnetic field forms network patches at the surface cell boundaries, while the pumping effect transport the weakest flux down towards the bottom of the CZ.

4.2. The kink instability

Fan et al. (1999) made 3-d non-convective simulations of buoyant kink-unstable flux ropes in a stratified atmosphere, and found that a twisted flux rope becomes significantly unstable only when the pitch α is well above a critical ideal value $\alpha_c = 1$, i.e. if $\psi_{\mathrm{R}} > 45^o$: in the resistive case α_c increases slightly. In 3D75 a kink therefore develops, with a maximum ideal growth rate $\Gamma_{\mathrm{kink}} \propto \tau_{\mathrm{A}}^{-1}(\alpha^2 - 1)$ (from Linton et al. 1998), yielding a characteristic time scale of $\Gamma_{\mathrm{kink}}^{-1} \approx 0.29\ \tau_{\mathrm{A}}$ significantly shorter than the rise time derived from the reference simulation. Diffusion decrease the growth rate further, but the instability still sets in rather quickly, well before the rope reaches the surface.

We do not invoke a perturbation of the rope's entropy, to onset the kink as in Abbett et al. (2000). Rather we let the rope be perturbed by the convective flows. The power of the convection at the initial position of the rope is predominantly at long wavelengths (100 Mm), and these wavelengths of the unstable kink modes dominate the rope's evolution.

When the rope (Fig 4.) approaches the surface, it contains adjacent mixed polarities in horizontal cross-sections; mpeg-movie.

4.3. Stable flux rope

In this case (3D45), the degree of twist is small enough to prevent the onset of the kink instability (the linear ideal growth rate vanishes for $\alpha = 1$, e.g. Fan et al. 1999), yet it is large enough to prevent the onset of the R-T instability. Thus, the rope retains its cohesion without distorting its shape by any of these two instabilities, and we may focus our attention on the effects of the convective flows on the rope.

Fig 6. compares our 3-d simulation to a corresponding 2-d convection-less reference simulation, and a simple analytic flux tube. As the 3-d rope rises, convective flows perturb its motion, preventing it from entering a rise phase with a constant rise speed, as in the reference simulation (see Fig 6a.) The rope remains straight and the maximum excursion of its axis, at the end of the simulation, is $\sim 0.04\ \lambda$. With the chosen super-equipartition axial field strength, the main action of the large-scale convective flows is to push the rope both left and right of the central plane (Fig 6b. — see also the mpeg-movie from the web-talk), while the effect of the small-scale downdrafts is to locally deform its equipartition boundary.

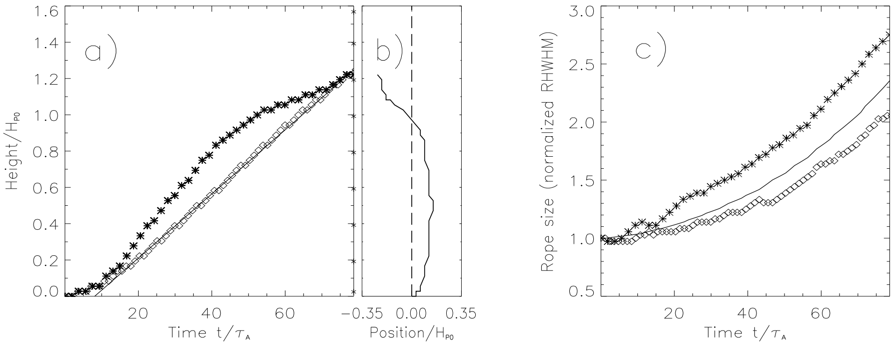

Figure 6. (a) Height of the flux rope as a function of time (stars). Also plotted are the corresponding results from a reference simulation (diamonds). The straight line corresponds to the average speed ($0.1\ v_{A0}$) in the rise phase. (b) Drift of the flux rope in the meridional plane. (c) Expansion of the flux rope (stars) with the corresponding result from the reference simulation over plotted (diamonds). Also plotted is an analytical expression (solid line, see text).

Initially the rope is located in a general updraft region. That explains why the rise speed of the rope is slightly greater than that of the reference simulation, which reaches a terminal speed of $\sim 0.1\ v_{A0}$. The 3-d rope also expands more quickly than the rope in the 2-d simulation, but its rate of expansion is close to what is expected from an adiabatically expanding, non-stretching tube with constant flux. Fig 6c. shows the rope's characteristic size R_{hwhm} defined by the average HWHM along its axis. As the rope rises and expands, its magnetic field strength also decreases at a rate close to that expected. The deviation can be attributed to the fact that, during its ascent, a significant amount of the magnetic flux within the 3-d rope is lost to its surroundings. This is illustrated in Fig 7. (left), that shows the total normalized magnetic flux within the rope's core Φ_i as a function of time for both the 2-d and 3-d ropes. As the 3-d simulation progresses, the total flux-loss from the computational domain is only 0.3% — the flux content of the rope, however, decreases more rapidly.

Also shown in Fig 7. (right) is the magnetic flux external to the rope Φ_e both above and below its center Φ_u and Φ_l respectively. Since the sum $\Phi_e + \Phi_i$ is nearly conserved, as Φ_i decreases, $\Phi_e = \Phi_u + \Phi_l$ must increase by an equal amount. However, the distribution of the flux-loss is not symmetric around the rope: more flux is lost to the surroundings below the rope than above.

This asymmetry also exists in the reference simulation, even though the total flux-loss is much smaller in that case. The asymmetry is a result of two factors. As the rope rises, the total volume above it decreases, while the volume below it increases. Furthermore, there is an anti-symmetry of the relative rise velocity across the rope: when the rope ascends, there is a tendency for flux to be advected towards it near its apex, and transported away from it in its wake. The

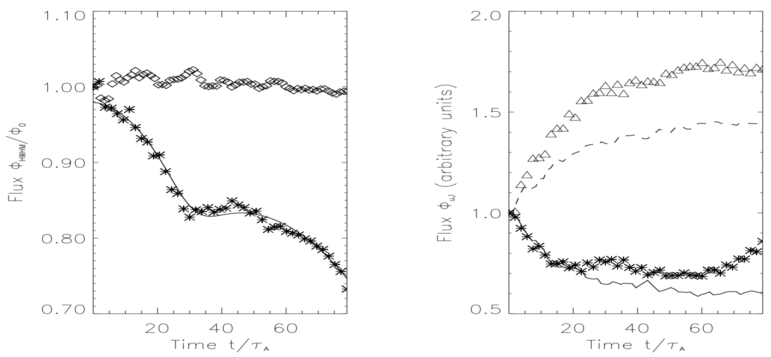

Figure 7. Left: magnetic flux within the rope Φ_i (stars), the corresponding quantity in the 2-d simulation (diamonds) and an analytic fit (solid curve), Right: the normalized flux outside and above the center of the 3-d rope Φ_u (stars), and below, Φ_l (triangles). The same quantities are shown for the 2-d reference simulation (solid and dashed curves respectively).

more pronounced asymmetry in the 3-d case can be attributed to the pumping effect that transports the weak field downwards (e.g. Dorch & Nordlund 2001).

We have defined the flux rope as the core magnetic structure that lies within the HWHM-boundary. This boundary is not, however, a contour that moves with the fluid in the classical sense: the flux within the latter kind of contour is naturally conserved (neglecting resistivity) and is equal to the total flux $\Phi_e + \Phi_i$. The HWHM-boundary is a convenient way of defining the flux rope and a characteristic size $\mathrm{R_{hwhm}}$, that behaves as it is expected to. The evolution of the flux within the rope's core Φ_i is determined by the integral of $\Delta\mathbf{v} \times \mathbf{B}$ along the rope's boundary, where $\Delta\mathbf{v}$ is the difference between the fluid velocity and the motion of the HWHM-boundary: the average "slip" Δv of the rope's boundary in the simulation is only a small fraction of the rise speed.

Making the rather crude assumptions that the boundary only moves radially relative to the fluid and that the circumference of the boundary is circular (which it is not), the flux-loss becomes

$$\dot{\Phi}_i = -\pi \mathrm{R_{hwhm}}\ \Delta v\ \mathrm{B}_c, \tag{2}$$

where B_c is the field strength at the center of the flux rope. Integrating the equation numerically with the quantities determined from the simulation the result is a good fit to the actual flux-loss, see Fig 7. (left) — if Δv is set to $3\ 10^{-4}\ v_{\mathrm{A}0}$ throughout the time span of the simulation except for a short interval of $\sim 3\ \tau_A$ around $t = 30\ \tau_{\mathrm{A}}$, where Δv changes sign, as the rope passes from one updraft to another (see below).

5. Discussion and Conclusions

The numerical simulations show that the interaction of a buoyant twisted flux rope with stratified convection leads to a magnetic flux-loss from the core of the rope. During the simulation, the flux rope rises 96 Mm, and loses about 25% of its original flux content. This, ceteris paribus, leads to a small increase in the amount of toroidal flux that must be stored at the bottom of the CZ during the course of the solar cycle.

Solar toroidal flux ropes rise about 200 Mm before emerging as bipolar active regions. One may thus expect them to lose even more of their initial flux, which would then be pumped back towards the bottom of the CZ. Moreover, the relative slip does not remain constant throughout the rope's rise. For example, Δv and hence $\dot{\Phi}_i$ changes at the time around $t = 30\ \tau_{\rm A}$, which corresponds to the time when the rope is at its maximum excursion from a vertical ascent (see Fig 6b.) At that time, the rope exits a convective updraft, and enters a different ascending "plume" to the left of the its original position. This leads to a transient compression of the rope. After entering the new plume, the average slip returns to its previous value for the remainder of the rise.

Petrovay & Moreno-Insertis (1997) suggested that turbulent erosion of magnetic flux tubes may take place due to the "gnawing" by turbulent convection: the flux tube is eroded by a thin current sheet forming spontaneously within a diffusion time. We do not find flux-loss via this type of enhanced diffusion, and rather, the flux-loss found here is entirely due to the advection of flux away from the core of the flux rope by convective motions. Most of the lost flux ends up in the rope's wake and some is mixed back into the upper layers. We speculate that both types of flux-loss may take place in the Sun, and as a result, the amount of toroidal flux stored near the bottom of the solar CZ may currently be underestimated.

Acknowledgments. EC-TMR supported the work through the ESMN. Computing time was provided by the Swedish National Allocation Committee.

References

Abbett, W.P., Fisher, G.H., & Fan, Y. 2000, ApJ, 540, 548

Caligari, P., Moreno-Insertis, F., & Schüssler, M. 1995, ApJ, 441, 886

Dorch, S.B.F. & Nordlund, Å. 1998, A&A, 338, 329

Dorch, S.B.F., Archontis, V., & Nordlund, Å. 1999, A&A, 352, L79

Dorch, S.B.F. & Nordlund, Å. 2001, A&A, 365, 562

Emonet, T. & Moreno-Insertis, F. 1998, ApJ, 492, 804

Fan, Y., Fisher, G.H., & McClymont, A.N. 1994, ApJ, 436, 907

Fan, Y., Zweibel, E.G., Linton, M.G., & Fisher, G.H. 1999, ApJ, 521, 460

Galsgaard, K. & Nordlund, Å. 1997, Journ. Geoph. Res., 102, 219

Linton, M.G., Dahlburg, R.B., Fisher, G.H., & Longcope, D.W. 1998, ApJ, 507, 404

Nordlund, Å., Galsgaard, K., & Stein, R.F. 1994, In R.J. Rutten, C.J. Schrijver (eds.), Solar Surface Magnetic Fields NATO ASI Series 433

Petrovay, K. & Moreno-Insertis, F. ApJ, 485, 398

Sterling, A.C., Hudson, H.S., Thompson, B.J., & Zarro, D.M. 2000, ApJ, 532, 628